Nanostructured ceria supported Pt and Au catalysts for the reactions of ethanol and formic acid

Aysegul Ciftci, D.A.J. Michel Ligthart, Pietro Pastorino, Emiel J.M. Hensen *

Schuit Institute of Catalysis, Eindhoven University of Technology, P.O. Box 513, 5600 MB Eindhoven, The Netherlands

ABSTRACT

Decomposition reactions of ethanol and formic acid were studied over a series of Au and Pt nanoparticle catalysts. CeO_2 nanorods and nanocubes served as model supports representing the $\{1\,1\,0\}$ and $\{1\,0\,0\}$ surfaces of CeO_2 nanocrystals. Pt was more active than Au in low temperature (below 400 °C) steam reforming, oxidation and decomposition (without an oxygen source) of ethanol. Similar trends were observed in the WGS reaction. Different from Au, for Pt the initial step of ethanol dehydrogenation to acetaldehyde is followed by the cleavage of the C—C bonds of acetaldehyde to CH_4 and CO due to the higher Pt—C bond strength when compared to that of Au—C. The catalysts supported on nanorod-shaped ceria were more active than those derived from nanocube-shaped ones in ethanol steam reforming and WGS reactions due to the abundance of OH species formed by activation of water on the oxygen vacancies in the $CeO_2\{1\,1\,0\}$ surfaces of ceria nanorod supported catalysts. Complete oxidation of ethanol to CO_2 and H_2O was observed over the Pt and Au supported CeO_2(rod) catalysts. For the former, complete oxidation took place starting from temperatures as low as 150 °C. These catalysts were active for decomposition of formic acid starting from near-ambient temperatures ($T > 50$ °C) up to 200 °C, at which temperature formic acid was completely converted over all the catalysts. Au was more active and it selectively dehydrogenated formic acid into CO_2 and H_2. The intrinsic activity of the CN-leached Au/CeO_2(rod) catalyst containing highly dispersed sub-nanometer Au clusters was higher than the parent catalyst. Pt, on the other hand, showed lower selectivity toward the dehydrogenation pathway due to its higher activity in WGS reaction and enhanced Pt—O bond strength resulting in decarbonylation of formic acid.

© 2012 Elsevier B.V. All rights reserved.

1. Introduction

Depletion of fossil fuels and the associated higher costs of these feedstocks in the future as well as environmental concerns related to their combustion have resulted in profound interest in alternative more sustainable energy resources. Therefore, the primary feedstock of the chemical industry is likely to shift from petroleum resources to renewable biomass [1–3]. Ethanol is a renewable feedstock which can be produced from carbohydrate biomass by fermentation. Through catalytic processes ethanol can be transformed into useful chemicals such as acetaldehyde, acetic acid, ethyl acetate, diethyl ether, ethylene oxide, ethylene and through aromatization of ethylene to aromatics like benzene and toluene [1,4,5]. Besides, ethanol is a suitable feedstock for the production of renewable hydrogen, which may become a clean energy carrier in the future. Hydrogen production from bio-ethanol may also become an integral part of future biorefineries because it can be used to upgrade certain biomass fractions [1,2]. Steam reforming of bio-ethanol to produce hydrogen is considered as a more sustainable alternative compared to steam reforming of non-renewable methane [6]. Bio-ethanol is obtained as an aqueous solution of ethanol, which can be almost directly used for steam reforming. The overall reaction of ethanol steam reforming is $C_2H_5OH + 3H_2O \rightarrow 2CO_2 + 6H_2$ [7,8]. Associated with steam reforming is the water-gas shift (WGS) reaction, which plays a key role in the generation of (additional) H_2 from CO [2,9,10]. Due to its easy handling and storage, ethanol is also considered as a promising green fuel for generation of hydrogen for use in H_2-fueled PEM fuel cells. Alternatively, it can be used as a reactant in direct ethanol fuel cells as a non-toxic, renewable alternative to direct methanol fuel cells [11,12].

Similar to ethanol, formic acid is also considered as an attractive liquid fuel for use in PEM fuel cells or in direct formic acid fuel cells (DFAFCs) [13]. Formic acid is generated as a by-product of levulinic acid production during the acid-catalyzed conversion of carbohydrates [14]. It has also been coined as an environmentally benign hydrogen storage material [13,15–17]. Formic acid can also be used as a hydrogen donor in transfer hydrogenation reactions [18,19]. As it is the simplest carboxylic acid, decomposition of formic acid is an interesting model

* Corresponding author. Tel.: +31 40 2475178; fax: +31 40 2455054.
 E-mail address: e.j.m.hensen@tue.nl (E.J.M. Hensen).

reaction to understand better the more complex chemistry of carboxylic acid conversion reactions. Biomass-derived carboxylic acids are potential feedstocks for obtaining clean hydrogen, fuel-grade alkanes and useful chemicals [1–3]. The decomposition of formic acid may proceed via decarboxylation (dehydrogenation), $HCOOH \rightarrow CO_2 + H_2$ with $\Delta G = -28.5$ kJ/mol or decarbonylation (dehydration), $HCOOH \rightarrow CO + H_2O$ with $\Delta G = -48.4$ kJ/mol. Decarbonylation is the dominant route in the gas phase in the absence of a catalyst. Studies on formic acid decomposition have been mostly concentrated on the use of homogeneous catalysis [15,16,20]. For the gas-phase decomposition of formic acid by heterogeneous catalysts, Rh supported on TiO_2, Al_2O_3, MgO and SiO_2 [21], Pt group metals supported on carbon [22], Au and Pt on Al_2O_3 [23], Pd and Au on carbon and TiO_2 [24], Au supported on SiO_2, carbon, CeO_2, Al_2O_3 and ZSM-5 [25] and supported Mo_2C catalysts [26] have been reported to be effective. Since CO-free H_2 is desired for fuel cell applications, the key point in formic acid decomposition would be to avoid formation of CO [13]. Accordingly, WGS activity of the formic acid decomposition catalysts is typically undesired.

CeO_2 is known to be a promising support for metal nanoparticles used to catalyze steam reforming of organic substances, reportedly because of ceria's involvement in the activation of water [27,28]. Recent works have emphasized that the surface plane of the ceria support on which the active metal phase is supported greatly influences its catalytic activity [29–32]. For instance, the group of Flytzani-Stephanopoulos showed that {1 1 0} surface planes of ceria support, the predominant surface on ceria with the nanorod morphology, are able to stabilize highly active Au nanoparticles for the WGS reaction, whereas {1 0 0} surface planes yield much less active catalysts [32]. Besides, Yi et al. showed that gold dispersed on CeO_2 nanorods showed excellent catalytic activity in low-temperature steam reforming of methanol, whereas Au deposited on CeO_2 nanocubes were inactive [29]. Besides, Au also Pt is very active in the WGS reaction [33–37]. As far as ethanol steam reforming is concerned, it is expected that Pt will outperform Au because the former is more active in C—C bond breaking reactions [38]. Although Au and Pt nanoparticle catalysts has received considerable attention in the conversion of ethanol [39–45] and formic acid [22–25] to useful chemicals and hydrogen, a comparison of the catalytic performances of Pt and Au supported on ceria and the effect of different crystal planes of the ceria support on the activity and selectivity of ethanol and formic acid conversion has not been reported yet. Therefore, we investigate the reaction pathways over Au and Pt catalysts supported on nanorod- and nanocube-shaped CeO_2 in ethanol (in the presence of O_2/H_2O and in the absence of an oxygen source) and formic acid decomposition reactions as well as in WGS reaction.

2. Experimental

2.1. Catalyst synthesis

CeO_2 nanorods and -cubes were synthesized according to the literature procedures [46]. Typically, 40 mL of 0.5 M $Ce(NO_3)_3$ aqueous solution and 60 mL of 10 M NaOH solution were added to a 125 mL Teflon-lined stainless steel autoclave. After stirring for 30 min, the autoclave was transferred to an oven and kept at 100 °C or 180 °C for 24 h to obtain CeO_2 nanorods or nanocubes, respectively. Thereafter, the precipitate was filtered and washed with deionized water until the pH of the filtrate was 7. Finally, the filtrate was dried at 110 °C overnight and calcined at 500 °C in static air for 4 h. The rod- and cube-shaped crystals are denoted by CeO_2(rod) and CeO_2(cube), respectively.

Platinum was loaded onto the ceria supports by pore volume impregnation using an aqueous $Pt(NH_3)_4(NO_3)_2$ solution. The CeO_2 support material was first sieved into a fraction of 125–250 μm and dried overnight at 110 °C. After impregnation, the materials were calcined in air at 450 °C for 2 h. Gold was introduced on the CeO_2 supports by homogeneous deposition-precipitation. To this end, a known amount of $HAuCl_4$ and urea were dissolved in 50 mL of water. 1 g of CeO_2 was added to this solution and mixed at 90 °C for 1 h. After filtration, washing and drying overnight at 110 °C, the catalyst was calcined at 400 °C for 2 h. A portion of the catalysts was treated with a cyanide-containing solution as outlined by Fu et al. [33]. An amount of catalyst was suspended in an aqueous solution of 2 wt.% NaCN solution. NaOH was added to keep the pH at 12. The mixture was stirred at room temperature for 2 h by bubbling O_2 through the solution. Subsequently, the resulting suspension was filtered, dried at 110 °C overnight and calcined at 400 °C for 4 h. The CN leached samples are denoted as Au/CeO_2(rod)-CN and Au/CeO_2(cube)-CN.

2.2. Catalyst characterization

The metal loading was determined by inductively coupled plasma atomic emission spectrometry (ICP-AES) analysis performed on a Goffin Meyvis Spectro Cirus^{ccd} apparatus. The samples were dissolved in a 3:1 HCl/HNO_3 solution by the addition of a few droplets of diluted H_2O_2.

Temperature programmed reduction (TPR) experiments were performed in a flow apparatus equipped with a fixed-bed reactor, a computer-controlled oven and a thermal conductivity detector. Typically, 30 mg catalyst was loaded in a tubular quartz reactor. Prior to TPR, the catalyst was oxidized by exposing to a flowing mixture of 4 vol.% O_2 in He by heating to the calcination temperature of the catalyst. After cooling down to room temperature in flowing N_2, the sample was reduced in 4 vol.% H_2 in N_2 at a flow rate of 8 ml/min, whilst heating from room temperature up to 800 °C at a ramp rate of 10 °C/min. The H_2 signal was calibrated using a CuO/SiO_2 reference catalyst.

Transmission electron micrographs were acquired on a FEI Tecnai 20 transmission electron microscope at an acceleration voltage of 200 kV with a LaB_6 filament. Typically, a small amount of sample was ground and suspended in pure ethanol, sonicated and dispersed over a Cu grid with a holey carbon film.

H_2-chemisorption was carried out at −80 °C using a Micromeritics ASAP 2020C setup [47]. Before analysis, an amount of sample was reduced from room temperature to 300 °C with a ramp rate of 2 °C/min for 2 h and evacuated at 435 °C. The double isotherm method was employed to determine the irreversibly bound chemisorbed hydrogen. To calculate the metal dispersion, an adsorption stoichiometry of one hydrogen atom per surface platinum atom was assumed. The accuracy of the analysis equipment was regularly verified by measuring a standard Pt/SiO_2 catalyst. The BET surface area was measured by nitrogen adsorption at −196 °C on a Micromeritics Tristar 3000 analyzer after drying the materials at 150 °C.

X-ray photoelectron spectroscopy (XPS) measurements were performed using a Kratos AXIS Ultra spectrometer, equipped with a monochromatic X-ray source and a delay-line detector (DLD). Spectra is obtained by using the aluminum anode (Al Kα = 1486.6 eV) operating at 150 W. Survey scans are measured at constant pass energy of 160 eV and region scans at 40 eV. The background pressure is kept at 2×10^{-9} mbar. Quasi-in situ XPS measurements were performed after reduction of the samples in a tubular quartz reactor with 10 °C/min heating rate from room temperature to 400 °C in a flow of 10 vol.% H_2 in He (total flow 100 ml/min). After cooling to room temperature, the lids at the inlet and outlet of the reactor were closed to prevent any interaction with air and the samples were prepared for XPS measurement in an Ar-flushed glove box.

2.3. Catalytic activity measurements

Ethanol decomposition experiments were carried out in a fixed bed plug flow reactor system. Typically, 50 mg of catalyst (sieve fraction 125–250 μm) diluted with 300 mg of α-Al_2O_3 was loaded into a stainless steel reactor with an internal diameter of 6 mm. Prior to reaction, the catalyst was reduced in a mixture 20 vol.% H_2 in N_2 at 400 °C for 2 h. Three types of feed compositions were used. The volumetric composition of these feed mixtures were C_2H_5OH:H_2O:He = 1:3:8, C_2H_5OH:O_2:He = 1:3:8 and C_2H_5OH:He = 1:11. In the case of ethanol steam reforming experiments the reactant feed mixture was obtained by evaporating ethanol and water in a He stream in two controlled evaporator mixers (Bronkhorst). All tubings were kept above 120 °C to avoid condensation of the reactants and products. The total gas flow rate was 150 ml/min and the GHSV was 15,000 ml_{EtOH}/g-cat h for all experiments. The reactor effluent was analyzed by online gas chromatography (Interscience GC-8000 Top, permanent gases on Shincarbon ST80/100 packed column connected to a TCD and hydrocarbons on a RT-Q bond column connected to a FID). The conversion (X) and carbon product selectivities (S_i) were calculated by:

$$X(\%) = \frac{\text{total C mol\%} - 2 \times \ \ C_2H_5OH \ \text{mol\%}}{\text{total C mol\%}} \times 100$$

$$S_i(\%) = \frac{\text{mol\% product}_i \times \text{number of C atoms}}{\text{total C mol\%} - 2 \times \ \ C_2H_5OH \ \text{mol\%}} \times 100$$

The H_2 selectivity and yield were calculated by:

$$S_{H_2}(\%) = \frac{\text{mol\% } H_2}{6 \times (\text{total C mol\%} - 2 \times \ C_2H_5OH \ \text{mol\%})/2} \times 100$$

$$Y_{H_2}(\%) = \frac{\text{mol\% } H_2}{6 \times (\text{total C mol\%})/2} \times 100$$

The catalytic activity in the WGS reaction was evaluated in a parallel ten-flow microreactor system [48]. Steam was supplied by evaporation of deionized water in a controlled evaporator mixer unit in combination with a liquid-flow controller and gas flows were controlled by mass flow controllers (Brooks and Bronkhorst). All tubings were kept above 100 °C after the point of steam introduction to avoid condensation. The dry product gas mixture was analyzed by an online gas chromatograph (Interscience CompactGC) equipped with Porapak Q (TCD) and Molecular sieve 5A (TCD) columns. Experiments were carried out in a mixture of 2.5 vol.% CO and 7.5 vol.% H_2O balanced by He at a dry GHSV of 9×10^4 h^{-1} (4×10^4 h^{-1} for the Au/CeO_2(rod)-CN sample) in the temperature range 135–400 °C. Typically, the catalyst was diluted with appropriate amount of SiC of the same sieve fraction. Prior to catalytic activity measurements, the catalyst was reduced in a flow of 20 vol.% H_2 in He at 300 °C followed by an isothermal period of 0.5 h. The reactor was cooled in He to the reaction temperature. The conversion of CO was calculated by dividing the mol% CO converted by the initial concentration of CO in the feed.

The catalytic decomposition of formic acid was investigated in a fixed bed plug flow reactor system. Typically, 50 mg of catalyst (sieve fraction 125–250 μm) diluted with 250 mg of SiC was loaded into a tubular quartz reactor. Prior to the reaction, the catalyst was reduced in a mixture of 20 vol.% H_2 in He for 2 h. The reactant feed mixture was obtained by leading 50 ml/min He through liquid formic acid kept at such temperature that a gas phase concentration of 5 vol.% was obtained. The composition of the effluent gas was analyzed by a Compact GC (Interscience) equipped with three channels. Formic acid was analyzed on a Stabilwax-DA column connected to a FID, CO_2 on a RT-Q-bond column connected to a TCD and
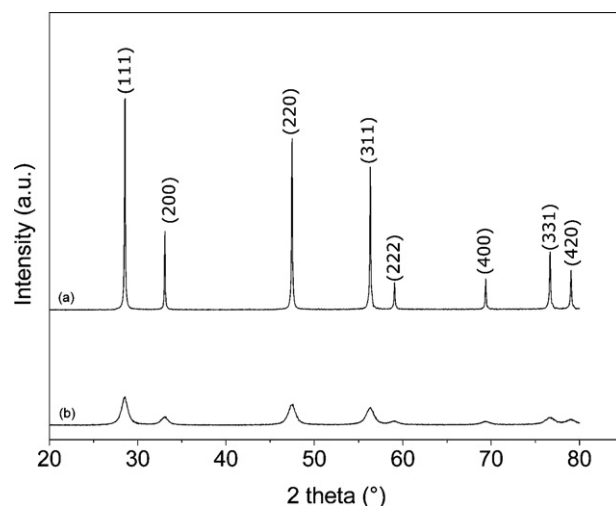

Fig. 1. X-ray diffraction patterns of (a) CeO_2 cubes and (b) CeO_2 rods.

CO and H_2 by a Molesieve-5A column connected to a TCD. The selectivity to CO_2 (H_2) was calculated by dividing the CO_2 concentration in the products to the sum of CO and CO_2 concentrations.

3. Results and discussion

3.1. Characterization of the catalysts

The XRD patterns in Fig. 1 evidence the crystalline nature of the CeO_2 supports. By use of Scherrer's equation, the particle size of the nanorods and -cubes was determined to be 10 and 75 nm, respectively. Representative transmission electron micrographs of these CeO_2 supports are shown in Fig. 2a–d. The d-spacing as determined from the electron micrographs is 0.30 nm. The nanorods have an average width of 8.5 nm and lengths between 30 and 150 nm. The nanocubes also exhibit a broad size distribution between 20 and 120 nm. The surface areas of the CeO_2(rod) and CeO_2(cube) samples were measured to be 130 and 14 m^2/g, respectively. The morphology of these nanostructured ceria supports is very similar to what has been reported in recent literature [29,30].

Table 1 lists the metal loading of the ceria-supported catalysts. In all cases, the metal content of the prepared catalysts is close to the targeted 2 wt.%. Cyanide leaching led to the nearly complete removal of Au from Au/CeO_2(cube). The gold content of Au/CeO_2(cube)-CN is below 0.01 wt.%. The gold content of Au/CeO_2(rod)-CN is substantially higher (0.09 wt.%) and corresponds quantitatively to an earlier report [30]. The different effect of cyanide leaching for nanorods and -cubes has been related to the stronger interaction of gold cations with the ceria {1 1 0} planes, which dominate the surface of the ceria nanorods, than with the

Table 1

Metal loading as determined by ICP analysis and the total hydrogen consumption during the H_2-TPR of ceria-supported catalysts.

Catalyst	Metal loading (wt.%)	n_{H_2} (μmol/g)	$(H_2/M)^a$
Pt/CeO_2(rod)	2.05	565	5.4
Pt/CeO_2(cube)	1.79	43	0.5
Au/CeO_2(rod)	2.14	416	3.8
Au/CeO_2(rod)-CN	0.09	514	n.d.[b]
Au/CeO_2(cube)	2.13	32	0.3
Au/CeO_2(cube)-CN	<0.01	60	n.d.
CeO_2(cube)	–	50	–
CeO_2(rod)	–	368	–

[a] H_2/metal (Au/Pt) ratio.
[b] Not determined.
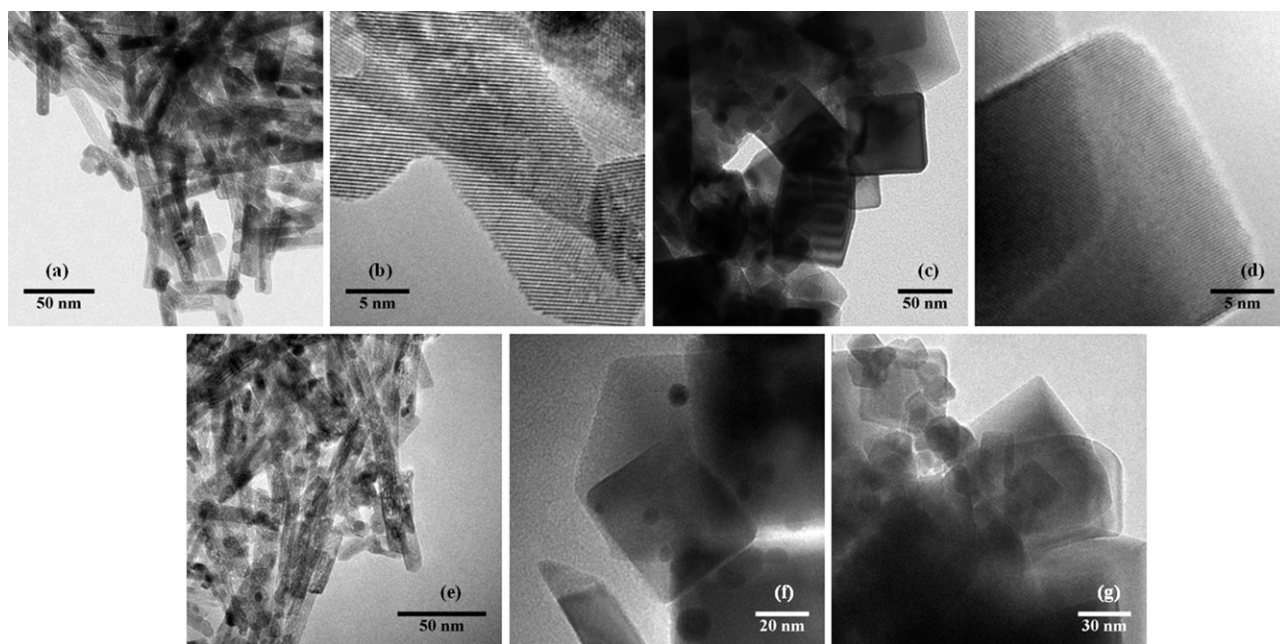
Fig. 2. TEM images of (a, b) CeO_2 rods, (c, d) CeO_2 cubes, (e) Au/CeO_2(rod), (f) Au/CeO_2(cube) and (g) Au/CeO_2(cube)-CN.

{1 0 0} planes of the ceria nanocubes. Cyanide leaching was not effective for removing a substantial fraction of Pt, despite the harsher leaching conditions (80 °C) employed for Pt/CeO_2 (results not shown). Transmission electron micrographs of the Au/CeO_2 catalysts are shown in Fig. 2e–g. The average sizes of the gold particles in Au/CeO_2(rod) and Au/CeO_2(cube) were 4.7 and 4.8 nm, respectively. Representative for Au/CeO_2(cube)-CN, Fig. 2g does not show gold nanoparticles in accordance with the negligible gold loading.

The reducibility of the various catalysts was evaluated by temperature programmed reduction (TPR). TPR profiles of Au/CeO_2, Pt/CeO_2 and the bare ceria supports are given in Fig. 3 and the amounts of consumed H_2 are collected in Table 1. In all cases, the H_2 consumption was higher for the catalysts based on nanorods than for those based on nanocubes. The difference is due to the lower reducibility of the ceria nanocube surface [30–32]. The


Fig. 3. TPR profiles of (a) Au/CeO_2(rod), (b) Au/CeO_2(rod)-CN, (c) Au/CeO_2(cube), (d) Au/CeO_2(cube)-CN, (e) Pt/CeO_2(rod), (f) Pt/CeO_2(cube), (g) CeO_2(rod) and (h) CeO_2(cube).

H_2-TPR profile of the bare CeO_2 nanorod support shows the commonly observed surface reduction feature around 550 °C followed by a H_2 evolution peak and, from 800 °C onwards, a peak due to bulk reduction [41,49–52]. This latter peak is also evident for CeO_2(cube), but its profile does not contain a clear separate peak for the reduction of the ceria surface. The TPR traces of the metal-containing samples look very different. They contain a strong feature at low temperature, which is due to reduction of the metal precursor and surface ceria reduction facilitated by spillover hydrogen from the metal [30,32,42,49]. The latter is evident from the high H_2/metal ratio (Table 1). The total amount of H_2 consumed is quite similar for Pt/CeO_2(rod), Au/CeO_2(rod) and Au/CeO_2(rod)-CN in line with the dominant part of H_2 consumption being the result of surface ceria reduction. Qualitatively, these trends are similar for the ceria nanocube catalysts with a lower total H_2 consumption. Note that the low temperature reduction peak for Au/CeO_2(cube)-CN indicates that this sample contains some residual gold which facilitate the reduction of the ceria surface at low temperature.

XP spectra of Au and Pt 4f regions of the fresh and reduced catalysts are shown in Fig. 4. The binding energy scales of all XP spectra were calibrated to the Ce 3d peak at 881.8 eV and the areas of all components were normalized against the area of Ce 3d envelope. The Au 4f spectra of Au/CeO_2(rod) and Au/CeO_2(cube) show that gold is predominantly present in the metallic state after calcination (BE = 83.4 eV). In the XP spectrum of Au/CeO_2(rod)-CN, this peak has shifted to higher binding energy (84.0 eV), which evidences that the small amount of Au left on the surface is cationic. After reduction at 400 °C, the binding energy shifts to 83.4 eV, indicating complete reduction of these gold cations. A previous investigation of leached Au/CeO_2 by means of X-ray Absorption Spectroscopy (XAS) [30] showed that fresh Au/CeO_2(rod) contains Au nanoparticles and a small amount of Au cations on the surface, whereas Au/CeO_2(rod)-CN only contains Au cations in close interaction with CeO_2, which are converted to very small Au clusters upon reduction at 250 °C.

A similar set of XP spectra of Pt/CeO_2(rod) and Pt/CeO_2(cube) and the corresponding fits are shown in Fig. 4e–h. The results of fitting these spectra with three different oxidation states for Pt, namely Pt^0, Pt^{2+} and Pt^{4+}, are collected in Table 2. The two fresh Pt/CeO_2(rod) catalysts mainly contain Pt-oxide. The Pt^0 content for Pt/CeO_2(cube) was higher. After reduction at 400 °C, the fraction
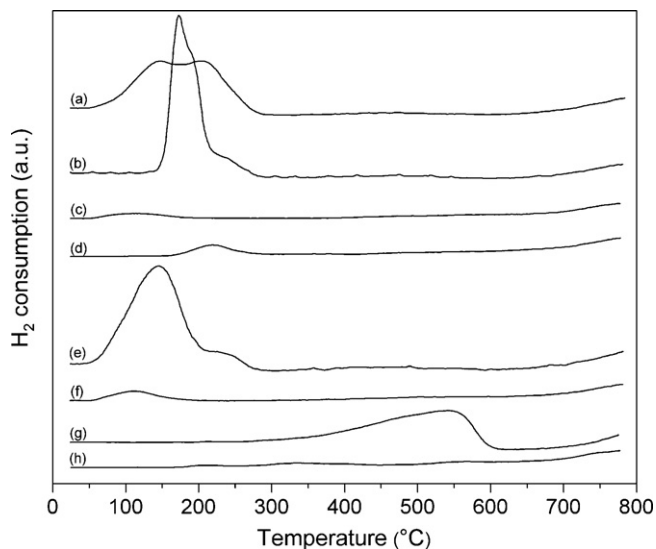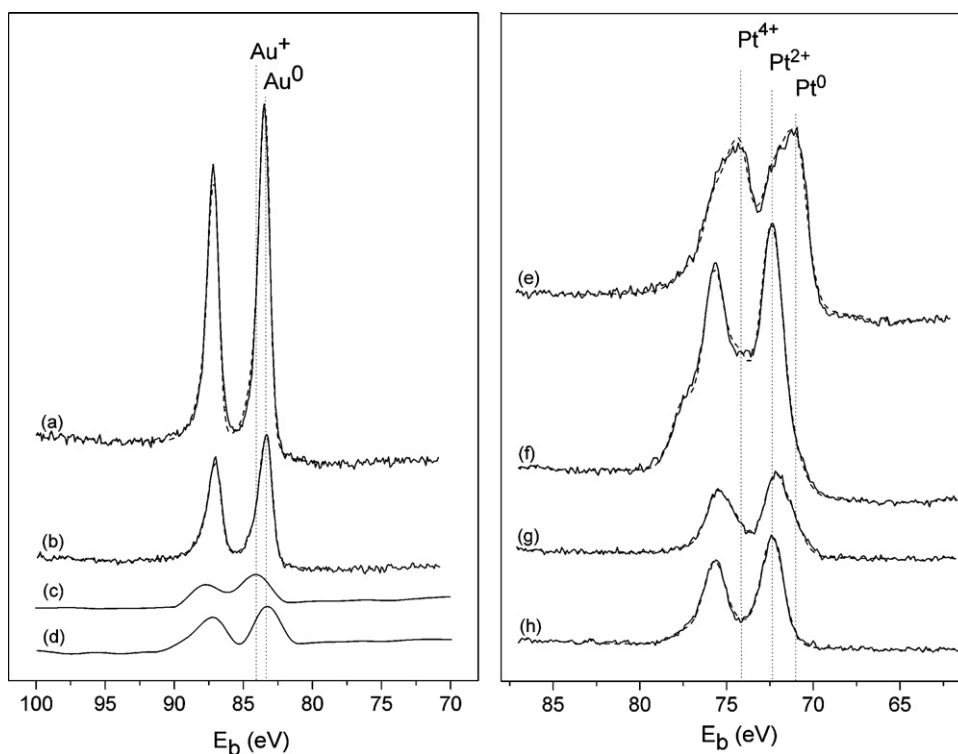
Fig. 4. XP spectra of Au 4f region of (a) calcined Au/CeO$_2$(cube), (b) calcined Au/CeO$_2$(rod) (c) calcined Au/CeO$_2$(rod)-CN (magnified 10 times), (d) calcined Au/CeO$_2$(rod)-CN after reduction at 400 °C (magnified 10 times), the positions of Au^0 and Au$^+$ 4f$_{7/2}$ are indicated; Pt 4f region of (e) calcined Pt/CeO$_2$(cube) after reduction at 400 °C, (f) calcined Pt/CeO$_2$(cube), (g) calcined Pt/CeO$_2$(rod) after reduction at 400 °C and (h) calcined Pt/CeO$_2$(rod), the positions of Pt^0, Pt^{2+} and Pt^{4+} 4f$_{7/2}$ are indicated. Full line represents the original spectra and dashed line represents the fitting.

of metallic Pt is 56% and 77%, respectively for Pt/CeO$_2$(rod) and Pt/CeO$_2$(cube). For the Pt/CeO$_2$(rod) sample a considerable amount of Pt with a 4f$_{7/2}$ binding energy of 72.4 eV was observed, which has been assigned to surface Pt associated with Ce^{3+} in a Pt–CeO$_x$ surface complex [53]. This shift to higher binding energies for Pt in Pt/CeO$_2$ catalysts has been reported previously in the literature [53,54] and it is mainly attributed to strong Pt–CeO$_2$ interactions [42,44,54–56], as is also evident from the difference in reducibility between Au/CeO$_2$ and Pt/CeO$_2$. These Pt^{2+} species are thought to be responsible for the high Pt dispersion on the ceria support. The Pt particle size in Pt/CeO$_2$(rod) and Pt/CeO$_2$(cube) were found to be 0.8 and 5.5 nm, respectively, by use of H$_2$ chemisorption taking into account the fraction of metallic Pt in these cases. The O 1s region of the metal-loaded CeO$_2$ nanorod and -cube catalysts (not shown here) evidence the presence of two oxidation states: one at 529.2 eV representing the oxygen anions of the ceria and one at 531.7 eV, appearing in some cases as a broad shoulder, attributed to hydroxyl groups on the surface. It has been reported that the peaks at 529.6, 530.3 and 532.7 eV are due to CeO$_2$, Ce$_2$O$_3$ and OH(a) (or some hydroxyl-containing oxide), respectively [57,58]. For all of the catalysts, reduction led to an increase of the hydroxyl species and a comparison of the spectra of nanorod and nanocube catalysts shows that the latter typically contains more of these hydroxyl groups than the former.

3.2. Catalytic activity measurements

3.2.1. Reactions of ethanol

With the purpose to obtain insight into the reaction mechanism, ethanol steam reforming was carried out at relatively low temperature (T < 400 °C) as compared to typical temperatures (600–800 °C) required to obtain complete conversion and high H$_2$ yields [7,8]. The results of ethanol steam reforming for the ceria-supported Pt and Au catalysts are collected in Table 3. It can be concluded that (i) the Pt catalysts are more active than the corresponding Au catalysts and (ii) catalysts derived from CeO$_2$(rod) are more active than those prepared using CeO$_2$(cube). The conversion of ethanol is almost complete for Pt/CeO$_2$(rod) at 400 °C. Under these conditions, the conversion is much lower for Pt/CeO$_2$(cube). At this temperature, the Au catalysts perform better than Pt/CeO$_2$(cube). The dominant product at 200 °C is acetaldehyde for both Pt and Au catalysts. With increasing temperature, the selectivity to CH$_4$, CO and CO$_2$ strongly increases for the Pt catalysts at the expense of the amount of acetaldehyde. At the highest temperature, the formation of acetone is also observed. Unlike these trends for Pt, the Au catalysts do not yield significant amounts of CH$_4$ or CO and acetaldehyde remains the main product at the highest temperature. Under these conditions, the selectivity to acetone is higher for Au than for Pt. From Table 3 it is seen that the CH$_4$ yield is

Table 2
Distribution of Pt oxidation states as determined from XPS measurements.

Catalyst	Pretreatment	Pt^0 (71.0 eV)	Pt^{2+} (72.4 eV)	Pt^{4+} (74.2 eV)
Pt/CeO$_2$(rod)	Fresh	1	87	12
	Reduced at 400 °C	56	43	1
Pt/CeO$_2$(cube)	Fresh	12	66	22
	Reduced at 400 °C	77	19	4

Table 3
Catalytic activity (conversion, selectivities and H_2 yield)[a] for ethanol steam reforming by Pt and Au catalysts supported on CeO_2 nanorods and nanocubes ($H_2O:C_2H_5OH$ = 3:1, 50 mg catalyst, GHSV = 15,000 ml_{EtOH}/g_{cat} h).

	Pt/CeO_2(rod)	Pt/CeO_2(cube)	Au/CeO_2(rod)	Au/CeO_2(cube)
200 °C				
X (ethanol)	4.3	2.0	1.3	0.2
S (acetaldehyde)	83	80	100	100
S (methane)	8.7	11	–	–
S (CO)	5.1	7.0	–	–
S (CO_2)	3.3	1.7	–	–
S (H_2)	23	20	–	–
Y (H_2)	1	0.4	–	–
300 °C				
X (ethanol)	30	9.0	4.8	3.3
S (acetaldehyde)	34	32	97	100
S (methane)	29	34	–	–
S (CO)	22	23	–	–
S (CO_2)	12	10	0.6	–
S (acetone)	0.8	–	2.6	–
S (ethyl acetate)	2.0	–	–	–
S (H_2)	21	23	20	15
Y (H_2)	6.5	2.0	1.0	0.5
400 °C				
X (ethanol)	99	14	31	16
S (acetaldehyde)	0.6	27	66	93
S (methane)	43	35	0.1	–
S (CO)	9.0	25	–	–
S (CO_2)	42	13	10	1.2
S (acetone)	3.4	–	24	4.0
S (ethyl acetate)	–	–	–	2.2
S (C_xH_y)[b]	1.6	0.2	0.1	–
S (H_2)	15	22	22	16
Y (H_2)	15	3.0	6.7	2.7

[a] X: conversion of ethanol (%); S: selectivities in C mol%; S (H_2): selectivity to hydrogen; Y (H_2): yield of hydrogen.

[b] Selectivity to C_2–C_3 alkanes and alkenes.

almost equal to the sum of CO and CO_2 yields for the Pt catalysts, the difference being due to the additional CO_2 formed together with acetone (vide infra). The trend of increasing (decreasing) methane (acetaldehyde) selectivity with temperature is consistent with a mechanism involving dehydrogenation of ethanol to acetaldehyde followed by its decomposition to CH_4 and CO through C—C bond cleavage [28,43,44,52,59–62]. Note that at these relatively low temperatures the reforming of CH_4 is very limited. CO_2 is produced from CO by the WGS reaction. Clearly, Au does not catalyze these C—C bond cleavage reactions, which is due to the much lower metal—carbon bond energy as compared to Pt [63]. Consequently, Au metal surfaces are only active in the dehydrogenation of ethanol to acetaldehyde. A major by-product of the reaction is acetone, whose selectivity strongly increases with the reaction temperature. For the Au/CeO_2 catalysts, we observed that the formation of acetone was accompanied by a decrease in acetaldehyde selectivity and at the same time the evolution of CO_2 and H_2. This is in agreement with the mechanism suggested by Nishiguchi et al. [64], that acetone formation proceeds through the transformation of acetaldehyde via aldol condensation, followed by the reaction of the aldol with lattice oxygen on CeO_2 to form the surface intermediate and its dehydrogenation and decarboxylation (overall reaction: $2C_2H_5OH + H_2O \rightarrow CH_3COCH_3 + CO_2 + 4H_2$). The involvement of water in these reactions toward acetone has also been reported [64]. Our results show that the rate of acetone formation is higher for the CeO_2(rod)-supported catalysts than for the CeO_2(cube)-supported ones (Table 3). The bare ceria supports exhibit a very low activity (conversion <1%) in ethanol steam reforming at 400 °C. The product mixture in this case consists of acetone, acetaldehyde, carbon dioxide and ethylene. For the CeO_2(rod) support, the major product is acetone, whereas the major product over the CeO_2(cube) is acetaldehyde. The Lewis acid sites formed by oxygen vacancies are likely the active sites for the condensation reactions toward acetone. The very low activities of

the bare CeO_2 supports confirm the importance of the metal for the initial dehydrogenation of ethanol to acetaldehyde in the formation of acetone. Gazsi et al. in their work on ethanol decomposition on Au/CeO_2 also reported that lower amount of products were desorbed from pure CeO_2 [45]. They concluded that the Au/CeO_2 interface plays an important role in the high activity of Au/CeO_2.

All of the catalysts showed stable activity at 200 and 300 °C, but tended to deactivate quite strongly at 400 °C. Especially, the activity of Pt/CeO_2(rod) decreased strongly from near complete ethanol conversion to a conversion of 15% after 6 h time on stream (Table S1). The deactivation led to a strong decrease of the amounts of CH_4 and CO concomitant with an increase of the amount of the acetaldehyde intermediate. Deactivation is most likely due to the rapid buildup of carbonaceous deposits on the Pt metal surface. It is observed that acetone formation is less hindered by deactivation of the Pt catalysts. This is likely because it takes place by reaction of acetaldehyde on the ceria surface. Besides, one should take into account that a smaller number of Pt surface atoms are expected to be involved in the dehydrogenation of ethanol to acetaldehyde than in the decomposition of acetaldehyde (the ensemble effect). It has also been suggested that accumulation of acetate species on the surface causes catalyst deactivation [42,65]. Although smaller, the deactivation of the Au nanoparticles is evident from the decreasing acetaldehyde and increasing acetone selectivity.

The catalytic performance of Pt/CeO_2(rod) and Pt/CeO_2(cube) in the WGS reaction are compared in Fig. 5a. Pt/CeO_2(rod) is significantly more active than Pt/CeO_2(cube). This result explains the higher CO_2 selectivity for Pt/CeO_2(rod) during ethanol steam reforming. For completeness, we also show the WGS performance of Au/CeO_2(rod) and Au/CeO_2(rod)-CN catalysts (Fig. 5b). Their performance is very similar to reported data [30]. Au/CeO_2(cube) has a very low activity in the WGS reaction. In the present work we establish that Au/CeO_2(rod) is already active in the WGS reaction below 200 °C. These Au data stress (i) the role of reduced gold
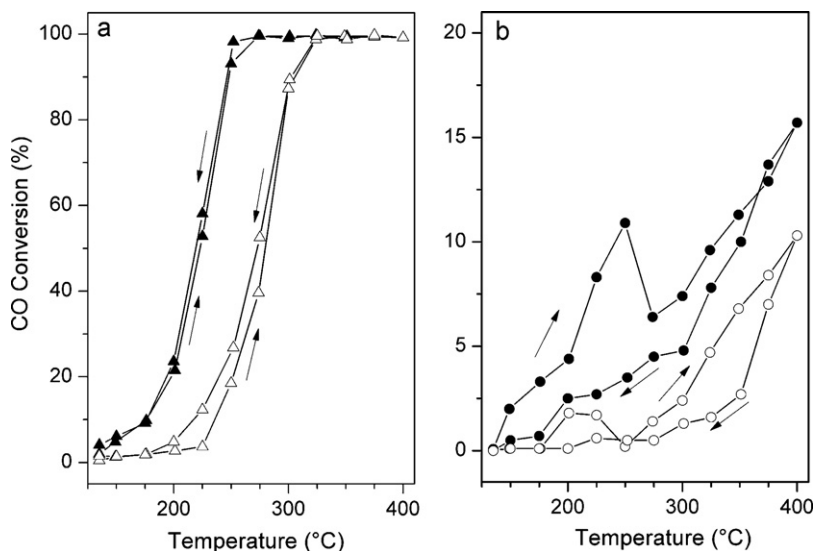
Fig. 5. WGS conversion for (a) $Pt/CeO_2(rod)$ (▲) and $Pt/CeO_2(cube)$ (△); and (b) $Au/CeO_2(rod)$ (●) and $Au/CeO_2(rod)$-CN (○) catalysts. The arrows indicate the increasing and decreasing temperatures during the experiments performed in a cycle.

particles, the finer dispersed the better, in the WGS reaction and (ii) the role of the ceria support in the activation of water. Comparison of the results of Au and Pt catalysts demonstrates that $Pt/CeO_2(rod)$ is significantly more active than $Au/CeO_2(rod)$. Pierre et al. have stressed the role of oxidized Pt species strongly bound to ceria in catalyzing the WGS [56]. The metal-support interface is suggested to provide an increased amount of surface oxygen species for the WGS reaction. On the other hand, one should also acknowledge that CO binds much more strongly to Pt than to Au [66].

The present data show that the $CeO_2(rod)$-supported samples are significantly more active in ethanol steam reforming and the WGS reaction than the $CeO_2(cube)$-supported ones. These differences are related to the better reducibility of the ceria nanorod support. It has been reported that the activation of water to adsorbed O and OH species is thermodynamically unfavorable on Pt surfaces [67]. The minimum bond energy of atomic O on a metal should be larger than 480 kJ/mol for H_2O dissociation to occur spontaneously ($H_2O_{(g)} \rightarrow OH_{ads} + \frac{1}{2}H_2$ and $H_2O_{(g)} \rightarrow O_{ads} + H_2$). Estimates for the binding energies of atomic O based on DFT calculations on Pt (354 kJ/mol) and Au (270 kJ/mol) are much lower than this minimum energy for spontaneous water dissociation [63]. Accordingly, the reaction rate for Pt surfaces may be limited by the low coverage of OH surface intermediates when oxygen-containing species are formed from steam. The activation of water on the vacancies in the ceria surface can also provide the hydroxyl species. The catalytic reactions may take place at the interface of the metal nanoparticles and the ceria surface or the OH species may migrate to the metal nanoparticles. Note, that the latter is more likely for Pt than for Au because of the higher metal–oxygen bond energy for the former. The TPR results show that Pt and Au facilitate the reduction of the ceria surface at relatively low temperature. This leads to the formation of O vacancies and Ce^{3+} surface sites, which are centers for water adsorption and activation [32,33,68–71]. Therefore, we can relate the higher activity of the $CeO_2(rod)$ derived catalysts to the higher H_2 consumption observed during TPR. This is in line with several reports evidencing the higher concentration of vacancies on $CeO_2(rod)$ compared to $CeO_2(cube)$ [29,32,72].

As they were the most active catalysts, $Pt/CeO_2(rod)$ and $Au/CeO_2(rod)$ were additionally tested for their activity in the oxidative and non-oxidative conversion of ethanol (Fig. 6). In the presence of O_2, $Pt/CeO_2(rod)$ completely oxidizes the ethanol feed

starting from temperatures as low as 150 °C. In contrast, ethanol conversion for $Au/CeO_2(rod)$ was complete only above 250 °C. Complete oxidation of ethanol over the Au/CeO_2 catalysts was previously reported by Haruta and co-workers [39]. CeO_2 is a good catalyst in oxidation reactions because of the formation of superoxide species on the defective ceria surface [39,73]. Petkovic et al. [74] suggested that O_2 is adsorbed at perimeter of the ceria surface and Pt nanoparticles, where ethanol is decomposed to carbon dioxide and water. In this case, it was argued that the support plays a role in the mobility of ethanol and its decomposed fragments on the support. The difference between Pt and Au in this particular case may also be partly due to the higher O surface coverage on Pt. The high activity in complete oxidation of ethanol at relatively low temperatures shows that $Pt/CeO_2(rod)$ and $Au/CeO_2(rod)$ are potent catalysts for the removal of volatile organic compounds (VOC) emitted from ethanol-fueled vehicles or other industries as well as in ethanol fuel cell applications [39,74]. The activity of $Pt/CeO_2(rod)$ increases in the order non-oxidative dehydrogena-
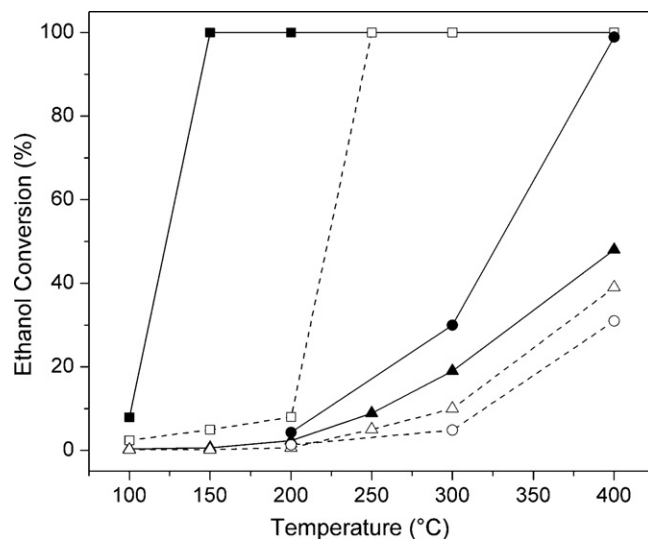
Fig. 6. Ethanol conversion with respect to temperature over $Pt/CeO_2(rod)$ (—) for a feed of $C_2H_5OH:O_2:He = 1:3:8$ (■), $C_2H_5OH:H_2O:He = 1:3:8$ (●) and $C_2H_5OH:He = 1:11$ (▲); and $Au/CeO_2(rod)$ (----) for a feed of $C_2H_5OH:O_2:He = 1:3:8$ (□), $C_2H_5OH:H_2O:He = 1:3:8$ (○) and $C_2H_5OH:He = 1:11$ (△).

Table 4
Comparison of product selectivities[a] and H_2 yield[b] for ethanol oxidation, ethanol steam reforming and ethanol decomposition experiments over Pt and Au catalysts supported on CeO_2 nanorods (50 mg catalyst, GHSV = 15,000 ml_{EtOH}/g_{cat} h).

	Pt/CeO_2(rod)			Au/CeO_2(rod)		
	$C_2H_5OH:H_2O$	$C_2H_5OH:O_2$	C_2H_5OH	$C_2H_5OH:H_2O$	$C_2H_5OH:O_2$	C_2H_5OH
300 °C						
S (acetaldehyde)	34	–	60	97	–	90
S (methane)	29	0.9	17	–	0.5	0.3
S (CO)	22	–	17	–	–	0.3
S (CO_2)	12	99	–	0.6	99	–
S (acetone)	0.8	–	0.7	2.6	–	–
S (ethyl acetate)	2.0	–	3.8	–	–	7.4
S(C_xH_y)[c]	–	–	1.5	–	0.8	1.9
S (H_2)	21	–	15	20	–	15
Y (H_2)	6.5	–	2.9	1.0	–	1.6
400 °C						
S(acetaldehyde)	0.6	–	75	66	–	72
S(methane)	43	0.2	0.9	0.1	1.0	0.6
S(CO)	9.0	–	1.5	–	–	1.0
S(CO_2)	42	99.8	1.7	10	98	2.7
S(acetone)	3.4	–	2.2	24	–	3.6
S(ethyl acetate)	–	–	2.1	–	–	3.1
S(acetic acid)	–	–	3.2	–	–	4.4
S(C_xH_y)[c]	1.6	–	9.0	0.1	0.5	12.4
S(others)[d]	–	–	4.4	–	–	0.5
S (H_2)	15	–	15	22	–	16
Y (H_2)	15	–	7.1	6.7	–	6.0

[a] S: selectivities in C mol%; S (H_2): selectivity to hydrogen.
[b] Y (H_2): yield of hydrogen.
[c] Selectivity to C_2—C_3 alkanes and alkenes.
[d] Selectivity to other products, mainly to diethyl ether.

tion < steam reforming < oxidative conversion. The main product of ethanol decomposition (in the absence of an oxygen source) is acetaldehyde (Tables 4 and S2). The activity in the presence is significantly higher, mainly because acetaldehyde is decomposed to CH_4 and CO. This points to a significant role of OH species generated on ceria in the decomposition of the acetaldehyde intermediate. The highest activity is obtained in the presence of O_2. Ethanol is totally combusted because of the high activity of O_2 on the ceria surface. Note, that the amount of acetone was also significantly lower during ethanol decomposition than during ethanol steam reforming. These results confirm the proposed role of water in the formation of acetone. For Au/CeO_2(rod) the activities in ethanol steam reforming and its non-oxidative dehydrogenation were similar. In both cases, the dominant product is acetaldehyde. These results are in keeping with results for reactions of ethanol on Au/CeO_2 reported by Gazsi et al. [45]. In that study it was also reported that the main process for the decomposition of ethanol was the dehydrogenation of ethanol and the addition of water did not improve the activity. This shows that, at least for Au, the dehydrogenation of ethanol is not catalyzed by OH groups on the ceria support. The much higher activity in the presence of O_2 is due to the activation of molecular oxygen on the ceria surface. Scheme 1 illustrates the mechanism of ethanol conversion over Pt and Au based CeO_2 catalysts.

3.2.2. Reactions of formic acid

The Pt and Au catalysts were also tested for their activity in the decomposition of formic acid in the temperature range 50–200 °C. Fig. 7a compares the conversion of the various catalysts as a function of the temperature. Au/CeO_2(rod) is the most active one in the temperature range 50–150 °C. The Au catalysts performed better than Pt catalysts in accordance with the results of Iglesia and Ojeda [23], who compared the activities of Au and Pt supported on Al_2O_3. At a temperature of 200 °C formic acid was completely converted by all of the catalysts. The selectivities in the decomposition of formic acid as a function of temperature are given in Fig. 7b. For Pt and Au catalysts the selectivity to CO_2 (H_2) is very high at temperatures below 75 °C. Below 75 °C, formic acid conversion is below 1% with a CO_2 (H_2) selectivity of 100%. However, above this temperature also CO was observed and in much greater amounts for Pt than Au. Solymosi et al. also reported in their study of formic acid decomposition on Pt group metals supported on carbon that CO-free H_2 generation could not be achieved. However, carbon (Norit)-supported Pt in that work (98% at 150 °C and 99.1% at 200 °C) gave a higher H_2 selectivity than our Pt/CeO_2 catalysts [22]. In the present study, the selectivity to CO was very low for Au. At 150 °C, CO_2 selectivities of Au/CeO_2(rod) and Au/CeO_2(cube) were 99.4% and 99.7%, respectively. The CO_2 selectivities of the Au/CeO_2 catalysts are higher than the equilibrium CO_2 selectivities in the
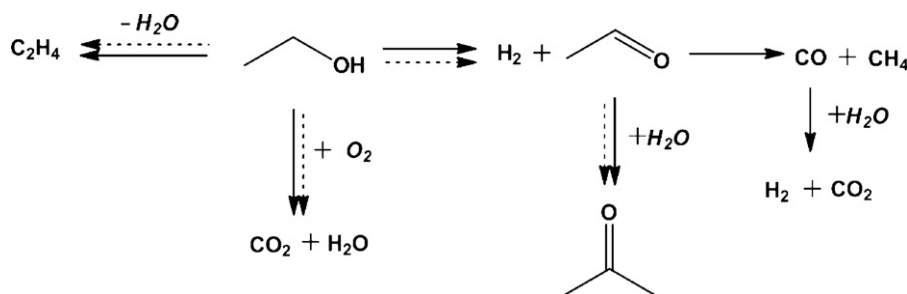
Scheme 1. The main reaction routes for ethanol conversion over the CeO_2 supported Pt (→) and Au (⋯→) catalysts.
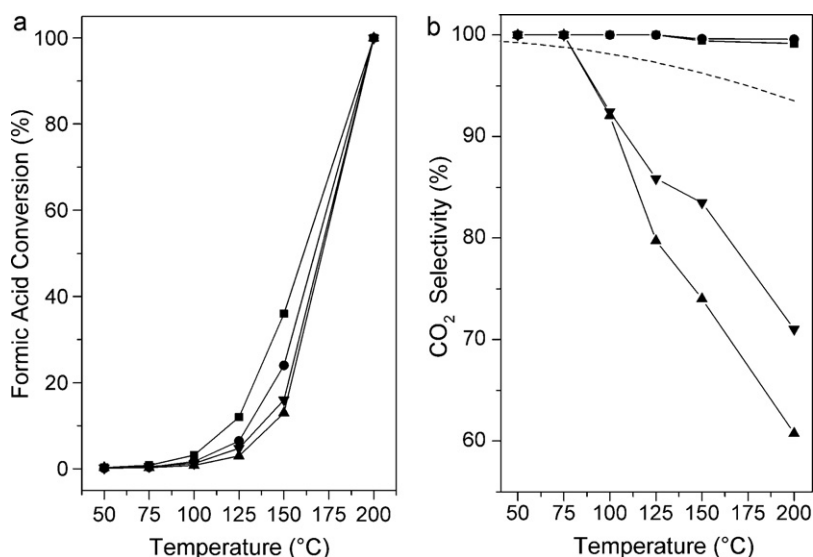
Fig. 7. Formic acid conversion (a) and CO_2 selectivity (b) obtained over Au/CeO$_2$(rod) (■), Au/CeO$_2$(cube) (●), Pt/CeO$_2$(rod) (▲) and Pt/CeO$_2$(cube) (▼). All catalysts reduced in H$_2$ at 250 °C. Dotted line represents the CO_2 selectivity values at the WGS equilibrium.

WGS reaction. These results show that the predominant pathway for formic acid decomposition over the Au/CeO$_2$ catalysts is decarboxylation and the WGS reaction is not involved in the reaction mechanism. As Au/CeO$_2$(rod) is already active in the WGS reaction below 200 °C (vide supra), one expects CO formation during formic acid decomposition. In contrast, at temperatures above 75 °C the CO_2 selectivities for the Pt/CeO$_2$ catalysts are below the equilibrium values for the WGS reaction, which evidences that the low CO_2 selectivity is not (only) due to the WGS reaction of CO_2 and H$_2$ but also due to decarbonylation of formic acid. In line with its higher WGS activity, Pt/CeO$_2$(rod) shows a lower selectivity to CO_2 than the Pt/CeO$_2$(cube) catalyst. The finding that decarbonylation occurs for Pt and not for Au relates to the stronger metal—oxygen bond energies for Pt, resulting in a higher activity in elementary reaction steps leading to an adsorbed OH surface intermediate (e.g. HCOOH$_{ads}$ → HCO$_{ads}$ + OH$_{ads}$). The work of Solymosi et al. suggested that the support choice may also influence the

selectivity of Pt nanoparticles [22]. In situ infrared spectroscopy studies of Beden et al. [75] showed that a substantial part of the Pt surface is covered by CO due to dissociative chemisorption of formic acid. Electrochemical studies show that Pt catalyzes formic acid oxidation by two pathways, namely via dehydrogenation and via dehydration. CO, the product of the dehydration pathway, will decrease the catalytic activity [76,77]. In contrast, Beltramo et al. [78] did not find any evidence for CO formation during the oxidation of formic acid on gold. The importance of surface formate as an intermediate (HCOO$_{ads}$) has been suggested in many previous studies. Typically, the stability of formate species is higher on Au than on Rh and Pt [21,22,25]. The catalytic activity of formic acid decomposition has also been related to the adsorption energy of CO. The adsorption energy of CO on Au particles is much weaker than on other transition metals. For instance, it has been argued that product CO strongly binds to Rh reducing the number of free Rh sites available for the dissociative adsorption of formic acid [25].
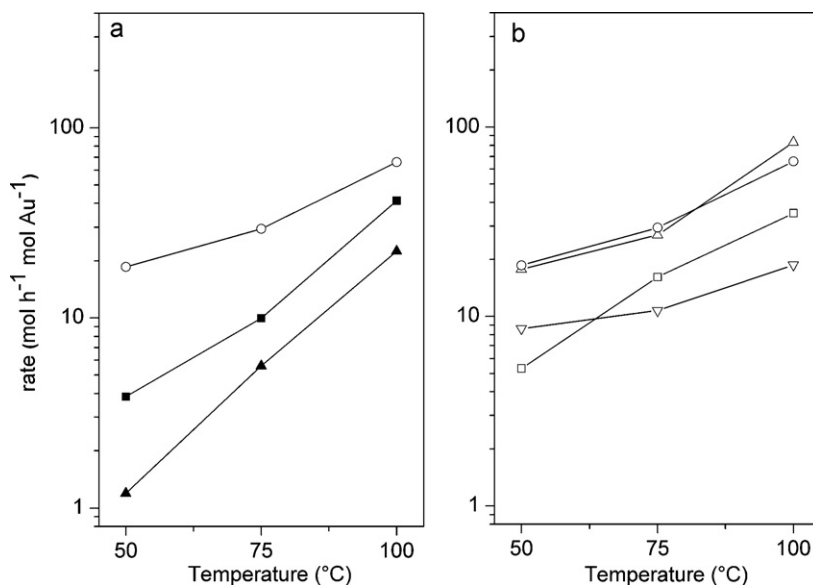
Fig. 8. Rates of formic acid decomposition over (a) Au/CeO$_2$(rod)-CN (○), Au/CeO$_2$(rod) (■) and Au/CeO$_2$(cube) (▲) after reduction in H$_2$ at 250 °C; (b) Au/CeO$_2$(rod)-CN dried at 120 °C (□), reduced at 150 °C (△), reduced at 250 °C (○) and reduced at 500 °C (▽).

Accordingly, the higher activity of Au than Pt may be argued to be the result of the stronger adsorption of product CO to the Pt surface.

Fig. 8a compares the rates of formic acid decomposition over $Au/CeO_2(rod)$, $Au/CeO_2(rod)$-CN and $Au/CeO_2(cube)$. The rate of formic acid dehydrogenation per mol of gold was the highest for the CN-leached catalyst, which contains sub-nanometer Au clusters. A similar observation was made for Au/Al_2O_3 by Iglesia and Ojeda [23]. These authors proposed that very small (TEM-invisible) Au clusters are the active sites in formic acid dehydrogenation at near-ambient temperatures. The gold phase in $Au/CeO_2(cube)$ mainly consists of reduced Au nanoparticles as evidenced by their complete removal upon cyanide treatment. By a similar argument as used by Iglesia and Ojeda, we suspect that the highly dispersed Au clusters in $Au/CeO_2(rod)$, which are present next to the Au nanoparticles, dominate the catalytic activity in formic acid decomposition. Accordingly, the activity of this catalyst is higher than that of $Au/CeO_2(cube)$. As a consequence of the removal of the low-activity gold nanoparticles, the intrinsic activity of the final $Au/CeO_2(rod)$-CN catalyst is much higher. Fig. 8b shows the influence of the pretreatment procedure of $Au/CeO_2(rod)$-CN on the rate of formic acid decomposition. After reduction in H_2 at 150 °C and 250 °C the activity of $Au/CeO_2(rod)$-CN is higher than the same catalyst dried in He at 120 °C. Clearly, reduced gold is required for formic acid decomposition. The activity of the catalyst reduced at 500 °C is much lower. These trends in activities are completely consistent with those reported for butadiene hydrogenation using a similar catalyst [30] and reinforce our conclusion that highly dispersed and metallic Au clusters are the active sites in formic acid decomposition. $Au/CeO_2(rod)$-CN reduced at 150 °C and 250 °C contains reduced subnanometer-sized Au clusters, whereas the sample dried in He at 120 °C mostly contains cationic Au species. The sample reduced at 500 °C contains somewhat larger Au nanoparticles as evidenced by EXAFS spectroscopy [30].

4. Conclusions

A set of Au and Pt supported CeO_2 nanorod and nanocube shaped catalysts were tested for their activity in the decomposition of ethanol and formic acid. Pt showed higher activity than Au in steam reforming of ethanol as well as its decomposition and oxidation. Besides, Pt was also found to be more active in the WGS reaction. In general, the nanorod-shaped CeO_2-supported catalysts are more active than nanocube-shaped ones. This difference relates to the higher activity of the former in the activation of water on oxygen vacancies in the CeO_2{1 1 0} surface, forming OH intermediates. For Pt and Au, the first step in ethanol conversion is its dehydrogenation to acetaldehyde. The higher ethanol steam reforming reaction rates on Pt are due to its ability to decompose acetaldehyde into CH_4 and CO. The higher C—C bond breaking activity of Pt stems from the higher Pt—C than Au—C bond strength. Accordingly, the main product on Au is acetaldehyde. Comparison to activity measurements without H_2O (ethanol decomposition) shows that water mainly facilitates the decomposition of acetaldehyde and not so much ethanol dehydrogenation. These catalysts are also very active for ethanol oxidation with Pt being preferred over Au. In formic acid decomposition Au is more active and selective toward H_2 than Pt catalysts. The selectivity of the Pt catalysts is lower because of their higher WGS activity compared to gold and decarbonylation as a primary reaction pathway. The latter is likely due to the higher Pt—O bond strength leading to an increased rate of dissociation of surface formate to CO. The results show that the high activity in the Au catalysts stems from highly dispersed sub-nanometer Au clusters.

Appendix A. Supplementary data

Supplementary data associated with this article can be found, in the online version, at http://dx.doi.org/10.1016/j.apcatb.2012.10.029.

References

[1] G. Centi, R.A. van Santen, Catalysis for Renewables: From Feedstock to Energy Production, Wiley-VCH, Weinheim, 2007.
[2] G.W. Huber, S. Iborra, A. Corma, Chemical Reviews 106 (2006) 4044–4098.
[3] A. Corma, S. Iborra, A. Velty, Chemical Reviews 107 (2007) 2411–2502.
[4] T. Takei, N. Iguchi, M. Haruta, Catalysis Surveys from Asia 15 (2011) 80–88.
[5] R. Barthos, A. Szechenyi, F. Solymosi, Journal of Physical Chemistry B 110 (2006) 21816–21825.
[6] N. Bion, F. Epron, D. Duprez, Catalysis 22 (2010) 1–55.
[7] A. Haryanto, S. Fernando, N. Murali, S. Adhikari, Energy and Fuel 19 (2005) 2098–2106.
[8] M. Ni, D.Y.C. Leung, M.K.H. Leung, International Journal of Hydrogen Energy 32 (2007) 3238–3247.
[9] J.D. Holladay, J. Hu, D.L. King, Y. Wang, Catalysis Today 139 (2009) 244–260.
[10] C. Song, Catalysis Today 77 (2002) 17–49.
[11] W. Zhou, Z. Zhou, S. Song, W. Li, G. Sun, P. Tsiakaras, Q. Xin, Applied Catalysis B: Environmental 46 (2003) 273–285.
[12] E. Antolini, Journal of Power Sources 170 (2007) 1–12.
[13] B. Loges, A. Boddien, F. Gartner, H. Junge, M. Beller, Topics in Catalysis 53 (2010) 902–914.
[14] D.J. Hayes, S. Fitzpatrick, M.H.B. Hayes, J.R.H. Ross, in: B. Kamm, P.R. Gruber, M. Kamm (Eds.), Biorefineries—Industrial Processes and Products, vol. 1, Wiley-VCH, Weinheim, 2006, p. 139.
[15] A. Boddien, B. Loges, H. Junge, M. Beller, ChemSusChem 1 (2008) 751–758.
[16] B. Loges, A. Boddien, H. Junge, M. Beller, Angewandte Chemie International Edition 47 (2008) 3962–3965.
[17] F. Joo, ChemSusChem 1 (2008) 805–808.
[18] R.A.W. Johnstone, A.H. Wilby, Chemical Reviews 85 (1985) 129–170.
[19] D.A. Bulushev, J.R.H. Ross, Catalysis Today 163 (2011) 42–46.
[20] C. Fellay, N. Yan, P.J. Dyson, G. Laurenczy, Chemistry: A European Journal 15 (2009) 3752–3760.
[21] F. Solymosi, A. Erdohelyi, Journal of Catalysis 91 (1985) 327–337.
[22] F. Solymosi, A. Koos, N. Liliom, I. Ugrai, Journal of Catalysis 279 (2011) 213–219.
[23] M. Ojeda, E. Iglesia, Angewandte Chemie International Edition 48 (2009) 4800–4803.
[24] D.A. Bulushev, S. Beloshapkin, J.R.H. Ross, Catalysis Today 154 (2010) 7–12.
[25] A. Gazsi, T. Bansagi, F. Solymosi, Journal of Physical Chemistry C 115 (2011) 15459–15466.
[26] A. Koos, F. Solymosi, Catalysis Letters 138 (2010) 23–27.
[27] Y. Li, X. Wang, C. Xie, C. Song, Applied Catalysis A: General 357 (2009) 213–222.
[28] L.V. Mattos, G. Jacobs, B.H. Davis, F.B. Noronha, Chemical Reviews 112 (2012) 4094–4123.
[29] N. Yi, R. Si, H. Saltsburg, M. Flytzani-Stephanopoulos, Applied Catalysis B: Environmental 95 (2010) 87–92.
[30] Y. Guan, D.A.J.M. Ligthart, O. Pirgon-Galin, J.A.Z. Pieterse, R.A. van Santen, E.J.M. Hensen, Topics in Catalysis 54 (2011) 424–438.
[31] J. Han, H.J. Kim, S. Yoon, H. Lee, Journal of Molecular Catalysis A: Chemical 335 (2011) 82–88.
[32] R. Si, M. Flytzani-Stephanopoulos, Angewandte Chemie International Edition 47 (2008) 2884–2887.
[33] Q. Fu, H. Saltsburg, M. Flytzani-Stephanopoulos, Science 301 (5635) (2003) 935–938.
[34] R. Burch, Physical Chemistry Chemical Physics 8 (2006) 5483–5500.
[35] D.C. Grenoble, M. Estat, D.F. Ollis, Journal of Catalysis 67 (1981) 90–102.
[36] R. Radhakrishnan, R.R. Willigan, Z. Dardas, T.H. Vanderspurt, AIChE Journal 52 (2006) 1888–1894.
[37] P. Panagiotopoulou, D.I. Kondarides, Catalysis Today 112 (2006) 49–52.
[38] A.V. Zeigarnik, R.E. Valdes-Perez, O.N. Myatkovskaya, Journal of Physical Chemistry B 104 (2000) 10578–10587.
[39] T. Takei, N. Iguchi, M. Haruta, New Journal of Chemistry 35 (2011) 2227–2233.
[40] Y. Guan, E.J.M. Hensen, Applied Catalysis A: General 361 (2009) 49–56.
[41] G. Jacobs, R.A. Keogh, B.H. Davis, Journal of Catalysis 245 (2007) 326–337.

[42] P. Ciambelli, V. Palma, A. Ruggiero, Applied Catalysis B: Environmental 96 (2010) 18–27.
[43] P. Ciambelli, V. Palma, A. Ruggiero, Applied Catalysis B: Environmental 96 (2010) 190–197.
[44] R.M. Navarro, M.C. Alvarez-Galvan, M. Cruz Sanchez-Sanchez, F. Rosa, J.L.G. Fierro, Applied Catalysis B: Environmental 55 (2005) 229–241.
[45] A. Gazsi, A. Koos, T. Bansagi, F. Solymosi, Catalysis Today 160 (2011) 70–78.
[46] H.X. Mai, L.D. Sun, Y.W. Zhang, R. Si, H.P. Zhang, H.C. Liu, C.H. Yan, Journal of Physical Chemistry B 109 (2005) 24380–24385.
[47] D.A.J.M. Ligthart, R.A. van Santen, E.J.M. Hensen, Journal of Catalysis 280 (2011) 206–220.
[48] D.A.J.M. Ligthart, R.A. van Santen, E.J.M. Hensen, Angewandte Chemie International Edition 50 (2011) 5306–5310.
[49] H.C. Yao, Y.F.Y. Yao, Journal of Catalysis 86 (1984) 254–265.
[50] B.B. Harrison, A.F. Diwell, C. Hallett, Platinum Metals Review 32 (1988) 73–83.
[51] L.A. Bruce, M. Hoang, A.E. Hughes, T.W. Turney, Applied Catalysis A: General 134 (1996) 351–362.
[52] J.Y. Siang, C.C. Lee, C.H. Wang, W.T. Wang, C.Y. Deng, C.T. Yeh, C.B. Wang, International Journal of Hydrogen Energy 35 (2010) 3456–3462.
[53] J.Z. Shyu, K. Otto, Journal of Catalysis 115 (1989) 16–23.
[54] A. Yee, S.J. Morrison, H. Idriss, Journal of Catalysis 191 (2000) 30–45.
[55] W. Lin, A.A. Herzing, C.J. Kiely, I.E. Wachs, Journal of Physical Chemistry C 112 (2008) 5942–5951.
[56] D. Pierre, W. Deng, M. Flytzani-Stephanopoulos, Topics in Catalysis 46 (2007) 363–373.
[57] E. Abi-aad, R. Bechara, J. Grimblot, A. Aboukais, Chemistry of Materials 5 (1993) 793–797.
[58] G. Praline, B.E. Koel, R.L. Hance, H.I. Lee, J.M. White, Journal of Electron Spectroscopy 21 (1980) 17–30.
[59] H. Idriss, Platinum Metals Review 48 (2004) 105–115.

[60] D.A. Morgenstern, J.P. Fornango, Energy and Fuel 19 (2005) 1708–1716.
[61] B. Zhang, W. Cai, Y. Li, Y. Xu, W. Shen, International Journal of Hydrogen Energy 33 (2008) 4377–4386.
[62] S. Ito, K. Tomishige, Catalysis Communications 12 (2010) 157–160.
[63] R.A. van Santen, M. Neurock, Molecular Heterogeneous Catalysis: A Conceptual and Computational Approach, Wiley-VCH, Weinheim, 2007.
[64] T. Nishiguchi, T. Matsumoto, H. Kanai, K. Utani, Y. Matsumura, W.J. Shen, S. Imamura, Applied Catalysis A: General 279 (2005) 273–277.
[65] A. Erdohelyi, J. Rasko, T. Kecskes, M. Toth, M. Domok, K. Baan, Catalysis Today 116 (2006) 367–376.
[66] C.D. Zeinalipour-Yazdi, A.L. Cooksy, A.M. Efstathiou, Surface Science 602 (2008) 1858–1862.
[67] M.A. Henderson, Surface Science Reports 46 (2002) 1–8.
[68] G. Jacobs, U.M. Graham, E. Chenu, P.M. Patterson, A. Dozier, B.H. Davis, Journal of Catalysis 229 (2005) 499–512.
[69] Q. Fu, S. Kudriavtseva, H. Saltsburg, M. Flytzani-Stephanopoulos, Chemical Engineering Journal 93 (2003) 41–53.
[70] R.J. Gorte, S. Zhao, Catalysis Today 104 (2005) 18–24.
[71] G. Jacobs, B.H. Davis, Catalysis 20 (2007) 122–285.
[72] M. Nolan, S.C. Parker, G.W. Watson, Physical Chemistry Chemical Physics 8 (2006) 216–218.
[73] T.X.T. Sayle, S.C. Parker, D.C. Sayle, Physical Chemistry Chemical Physics 7 (2005) 2936–2941.
[74] L.M. Petkovic, S.N. Rashkeev, D.M. Ginosar, Catalysis Today 147 (2009) 107–114.
[75] B. Beden, A. Bewick, C. Lamy, Journal of Electroanalytical Chemistry 148 (1983) 147–160.
[76] J.D. Lovic, A.V. Tripkovic, S.L.J. Gojkovic, K.D. Popovic, D.V. Tripkovic, P. Olszewski, A. Kowal, Journal of Electroanalytical Chemistry 581 (2005) 294–302.
[77] N. Kristian, Y. Yan, X. Wang, Chemical Communications 3 (2008) 353–355.
[78] G.L. Beltramo, T.E. Shubina, M.T.M. Koper, ChemPhysChem 6 (2005) 2597–2606.